Superconductivity and spin fluctuations in the actinoid–platinum metal borides {Th,U}Pt_3B

E. Bauer,[1] E. Royanian,[1] H. Michor,[1] O. Sologub,[1] E.-W. Scheidt,[2] A. P. Gonçalves,[3] J. Bursik,[4] W. Wolf,[5,6] D. Reith,[5,6] C. Blaas-Schenner,[6] R. Moser,[6] R. Podloucky,[6] and P. Rogl[6]

[1]*Institute of Solid State Physics, Vienna University of Technology, A-1040 Wien, Austria*
[2]*Chemische Physik und Materialwissenschaften, Universität Augsburg, D-86159 Augsburg, Germany*
[3]*C2TN, Instituto Superior Tecnico, Universidade de Lisboa, 2695-066 Bobadela LRS, Portugal*
[4]*Institute of Physics of Materials, Academy of Sciences of the Czech Republic, 61662 Brno, Czech Republic*
[5]*Materials Design, S.A.R.L. 18 rue de Saisset, 92120 Montrouge, France*
[6]*Institute of Physical Chemistry, University of Vienna, A-1090 Wien, Austria*

(Received 6 May 2015; published 24 July 2015)

Investigating the phase relations of the system {Th,U}-Pt-B at 900 °C the formation of two compounds has been observed: cubic $ThPt_3B$ with $Pm\bar{3}m$ structure as a representative of the perovskites, and tetragonal UPt_3B with $P4mm$ structure being isotypic to the noncentrosymmetric structure of $CePt_3B$. The crystal structures of the two compounds are defined by combined x-ray diffraction and transmission electron microscopy. Characterization of physical properties for $ThPt_3B$ reveals a superconducting transition at 0.75 K and an upper critical field at $T = 0$ exceeding 0.4 T. For nonsuperconducting UPt_3B a metallic resistivity behavior was found in the entire temperature range; at very low temperatures spin fluctuations become evident and the resistivity $\rho(T)$ follows non-Fermi liquid characteristics, $\rho = \rho_0 + AT^n$ with $n = 1.6$. Density functional theory (DFT) calculations were performed for both compounds for both types of structures. They predict that the experimentally claimed cubic structure of $ThPt_3B$ is thermodynamically not stable in comparison to a tetragonal phase, with a very large enthalpy difference of 25 kJ/mol, which cannot be explained by the formation energy of B vacancies. However, the presence of random boron vacancies possibly stabilizes the cubic structure via a local strain compensation mechanism during the growth of the crystal. For UPt_3B the DFT results agree well with the experimental findings.

DOI: 10.1103/PhysRevB.92.024511 PACS number(s): 74.25.Bt, 74.70.Ad, 72.15.Eb

I. INTRODUCTION

The discovery of $CePt_3Si$ ($CePt_3B$ type) as the first heavy fermion superconductor without a center of inversion [1] has triggered widespread research activities to search for superconducting states in related ternary or quaternary alloy systems [2]. Therefore, our studies were extended to actinoid metal–platinum metal–boride systems searching for materials with similar property characteristics and/or a possibly high Seebeck effect due to strong electron correlations. The aims of the present research are (i) a detailed investigation of phase relations in the systems An-Pt-B near the composition $AnPt_3B$, (An = Th,U), (ii) the evaluation of the crystal structures of ternary compounds, and (iii) the characterization of physical properties of materials. This paper summarizes various results on the compounds $ThPt_3B$ with cubic and UPt_3B with tetragonal crystal structure.

II. EXPERIMENT

Alloys $AnPt_3B$, An = Th,U (1.5 gram each) were prepared by argon arc melting on a water-cooled copper hearth in Ti-gettered argon from elemental ingots with a minimal purity of 99.9 mass%. All alloys were sealed in quartz tubes and annealed. The stability of the $ThPt_3B$ phase was investigated in long term annealing experiments at 800 °C (500 h), 600 °C (1000 h), and 400 °C (2500 h), but no changes in the x-ray intensities and crystal symmetry were observed. A CAMEBAX SX50 wavelength dispersive spectrograph (PC-3 spectrometer crystal for B K_α) was employed for composition analyses. Although with careful calibration of the soft B K_α radiation in ThB_4 and Pt_3B_2, boron was unambiguously detected in the $AnPt_3B$ compounds (as well as an An/Pt ratio of 3); quantitative composition analyses of the B content in combination with the heavy elements Th/U and Pt indicated a B content of about 15 ± 5 at. % B.

X-ray powder diffraction data from as-cast and annealed alloys were collected on a Guinier-Huber image plate system with Cu $K_{\alpha 1}(8 < 2\Theta < 100°)$. Refinement of the crystal structures was performed with the program FULLPROF [3]. A Philips CM12 STEM transmission electron microscope (TEM) was used with an EDX analyzer and Phoenix software to corroborate unit cell, symmetry, and formation of superstructures. TEM investigations were performed on particles 0.1–2 μm, which were obtained by mechanically crushing alloy pieces under ethanol and transferring the particles on a thin holey carbon film supported by a copper grid. It turned out that isolated particles on a carbon film with little means of heat transfer often melted under the electron beam, which made work very difficult. Hence alternatively samples for TEM were prepared in the form of thin lamellae (lateral dimensions about 10 × 7 μm) perpendicular to the polished facet of a material fragment using a focused ion beam (FIB) technique in a TESCAN LYRA 3 XMU FEG/SEM × FIB scanning electron microscope. Measurements of the various physical properties were carried out with a series of standard techniques [4]. Low temperature specific heat experiments were performed in a $^3He/^4He$-dilution refrigerator down to a base temperature of 60 mK using a standard relaxation method [5].

III. COMPUTATIONAL DETAILS

Density functional theory (DFT) calculations were performed by applying the Vienna *Ab-initio* Simulation

Package (VASP) [6,7] utilizing the pseudopotential construction according to the projector-augmented-wave method [8]. For the exchange-correlation functional the local-density approximation (LDA) of Ceperley and Alder [9] as parametrized by Perdew and Zunger [10] was chosen. The Brillouin-zone integration on an $11 \times 11 \times 11$ $\vec{k}$-point mesh [11] was made by a Gaussian smearing technique for a smearing parameter of $\sigma = 0.2$ eV. Structural parameters were fully optimized and the electronic structure was calculated scalar-relativistically (i.e., omitting spin-orbit coupling) as well as fully relativistically including spin-orbit coupling [12].

For vibrational properties within the harmonic approximation we used the direct force-constant method as implemented in the program package fPHON [13]. For deriving the force constants atomic displacements of 0.02 Å were chosen. Before applying such displacements the structural parameters (i.e., the volume and shape of the unit cell as well as the positions of the atoms within the unit cell) were relaxed until the residual forces were less than 10^{-4} eV/Å. Anharmonic vibrational properties were calculated by means of the self-consistent *ab initio* lattice dynamics (SCAILD) method [14,15].

IV. RESULTS AND DISCUSSION

A. Phase relations

Phase equilibria in the An-Pt-B systems were explored in the region for less than 34 at. % An at 900 °C, revealing a series of ternary compounds of which compounds with the composition close or at $ThPt_3B$ and UPt_3B were those with the lowest boron content. Homogeneous regions, if any, are certainly small, as unit cell parameters were not found to change significantly in ternary alloys. In related An-Pd-B systems, neither isotypic UPd_3B nor isotypic $ThPd_3B$ were found in our earlier investigations [16].

B. Crystal structure of $ThPt_3B$

Single crystals were isolated from the mechanically crushed alloy with nominal composition $ThPt_3B$ and showed a cubic primitive unit cell corresponding to $a = 0.4383(2)$ nm. X-ray intensities confirmed isotypism with the filled $AuCu_3$ type structure, space group $Pm\bar{3}m$, i.e., a perovskite boride with Th atoms at the corners and Pt atoms at the face-centered positions of the cubic unit cell. For the boron atoms the sites in the center of the unit cell are the most likely ones, similar to isotypic $CePt_3B$ (see Fig. 1). The weak x-ray scattering power of boron atoms, however, may mask the true boron content and a random distribution of boron atoms with a certain amount of vacancies in the site 1a is likely, as also indicated by the large value of the residual resistivity (see Fig. 4). Crystal symmetry and unit cell dimensions are fully confirmed by TEM analyses (see section below).

DFT calculations predict that the tetragonal structure is by 25 kJ/mol more stable than the cubic one (compare Tables I and II). It is well known that B has a strong tendency to distort high symmetry structures and form a huge variety of more or less distorted structural patterns. The strong preference for the tetragonal structure was also predicted by DFT for first row elements from H to N at the position of B. Further DFT tests were performed by shifting B a few

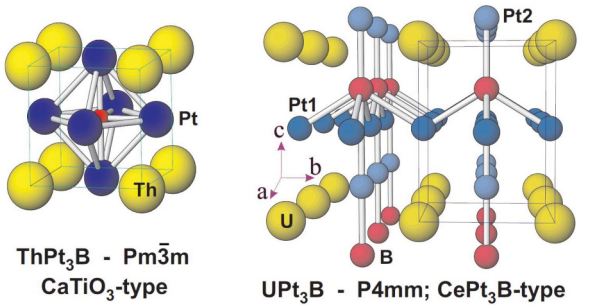

FIG. 1. (Color online) View of the crystal structures of $ThPt_3B$ and UPt_3B.

10^{-2} Å away from its high symmetry position and allowing VASP for automatic structural optimization. All these calculations led to the tetragonal structure without any energy barrier. Numerous DFT calculations including vacancies up to 25% but trying to maintain a cubic (or slightly distorted cubic) structure led to the same conclusion, namely that the cubiclike environment for B is unfavorable. In fact, removing B totally is always energetically more favorable than including it in a cubic framework as illustrated also by the enthalpy difference in the last column of Table II and the energy differences are indeed very large.

Removing B totally results in a volume reduction of more than 10 Å^3/atom for the unit cell of $ThPt_3\square$ according to Table II. The reduction of the lattice parameter would be 0.197 Å for 100% B vacancies. Due to the LDA error the uncertainty in the cubic lattice parameter is too large for a precise estimation of B vacancies. Vacancy concentrations of about 5%–10% are within the accuracy limit.

More elaborate calculations were done involving the cluster expansion plus Monte Carlo technique [17] studying the temperature dependent energetics for B vacancies at higher concentrations. However, the large enthalpy difference between the tetragonal and the idealized cubic structure could by far not be overcome by vacancy formation.

Therefore, after all these experimental and computational efforts the conclusion can only be that the experimental sample of $ThPt_3B$ has cubic structure with a small amount (up to 10%) of B vacancies. As already suggested during the growth of the crystal the formation of the cubic structure is possibly enforced by a local strain compensation mechanism as described in Ref. [18] for the suppression of the phase transformation in binary rare earth dicarbides.

TABLE I. Structural parameters for compounds with the tetragonal structure in space group $P4mm$: lattice parameters a, c as well as volume per atom V_0. The z parameters as calculated by DFT (with $z_{Pt2} = 0$ in both cases) are as follows: for $ThPt_3B$ $z_{Th} = 0.161$, $z_{Pt1} = 0.618$, and $z_B = 0.414$; for UPt_3B $z_U = 0.169$, $z_{Pt1} = 0.618$, and $z_B = 0.406$.

	Method	a (nm)	c (nm)	V_0 (Å^3/atom)
UPt_3B	Expt	0.38906	0.52241	15.82
UPt_3B	DFT	0.3821	0.5225	15.25
$ThPt_3B$	DFT	0.3936	0.5194	16.09

TABLE II. Structural parameters a and volume per atom V_0 for the compounds with cubic space group $Pm\bar{3}m$ with and without boron. Last column, upper block: total energy difference of cubic structure relative to tetragonal structure $\Delta H_{\text{cub-tet}}$. By this amount the cubic structure is less stable than the tetragonal one. Last column, lower block: total energy difference of cubic structures without and with boron. By this amount the $AnPt_3B$ compound is less stable than $AnPt_3$+ solid B.

	Method	a (nm)	V_0 (Å^3/atom)	$\Delta H_{\text{cub-tet}}$ (kJ/mol)
$ThPt_3B_{(1-\delta)}$	Expt	0.4383	16.84	
$ThPt_3B$	DFT	0.4355	16.52	25.09
UPt_3B	DFT	0.4298	15.88	35.41
		a (nm)	V_0 (Å^3/atom)	$\Delta H_{\text{withB-noB}}$ (kJ/mol)
$ThPt_3\square$	DFT	0.4158	14.38	18.72
$UPt_3\square$	DFT	0.4067	13.45	21.52

C. Crystal structure of UPt_3B

Single crystals isolated from the mechanically crushed alloy indicated a tetragonal primitive unit cell with $a = 0.38906(3)$ and $c = 0.52241(5)$ nm. The x-ray intensity spectrum indicated isotypism with the $CePt_3B$ type structure. This structure type lacks a center of symmetry and is also adopted by the heavy fermion superconductor $CePt_3Si$ [1]. From the refinement data the correspondence of U and Ce atoms, and Si and B atoms is straightforward: space group $P4mm$, U in $1b$ [$\frac{1}{2}$, $\frac{1}{2}$, $z = 0.1621(6)$], Pt1 in $2c$ [$\frac{1}{2}$, 0, $z = 0.6134(8)$], Pt2 in $1a$ [0, 0, 0 (fixed)], and B in $1a$ [0, 0, $z = 0.3521(10)$]; see Fig. 1. The low residual value, $R_F = 0.036$ for 55 reflections in a Rietveld refinement, confirms the structure type.

With the exception of the position of B the DFT results in Table I are in good agreement with the experimental data. The DFT derived volume per atom is about 3.5% smaller than the measured value which is attributed to the LDA approximation. Also the values for the z coordinate of U and Pt compare well with experiment. A sizable discrepancy occurs for the z parameter of B (experiment: $z = 0.3521$; DFT: $z = 0.406$). Several DFT tests were made including also the application of an exchange-correlation functional of the general-gradient-approximation type [19]. Within fluctuations of 1% of the z parameter its result was always the same.

D. Transmission electron microscopy of $ThPt_3B$ and of UPt_3B

Grains of $ThPt_3B$ and UPt_3B were identified via the internal EDX system of the TEM apparatus. A series of selected area diffraction (SAD) patterns was then taken at various sample tilts. Figure 2 summarizes the most representative diffraction patterns obtained on $ThPt_3B$ with low index zone axes [100], [110], [111], and [211] and their simulations using software JEMS [20]. Similarly, Fig. 3 contains low index diffraction patterns with zone axes [100], [101], [110], and [001] plus their simulations for UPt_3B. All diffraction patterns were fully indexed using the lattice parameters found by x-ray diffraction techniques. No superstructure spots were detected confirming the crystal system and the unit cell dimensions given above. The observed intensities of diffraction spots correlate well with the simulations based on the atomic positions presented.

The crystal structures of $ThPt_3B$ and UPt_3B are shown in Fig. 1 in three-dimensional view and reveal the close relationship of UPt_3B being a noncentrosymmetric distorted variant of cubic perovskite $ThPt_3B$. Tables I and II present the experimentally observed and calculated structural parameters for both $ThPt_3B$ and UPt_3B.

E. Superconductivity of $ThPt_3B$

Measurements of the temperature dependent electrical resistivity carried out at low temperatures down to 0.05 K reveal a superconducting transition around 0.75 K, if the resistivity drop taken at 50% is considered (compare Fig. 4). The application of a magnetic field suppresses T_c with an initial slope of about -0.83 T/K, extrapolating to an upper critical field at $T = 0$ well below 1 T. The almost linear dependency of $\mu_0 H'_{c2}(T)$ in Fig. 5 refers to some deviation of the upper critical field from the standard WHH-type behavior [21]. The temperature dependent resistivity in the normal state region does not comply with a simple metallic dependence; rather, $\rho(T)$ shows a negative temperature coefficient, reminiscent of $TmPt_{\sim 3}Si$ [22]. Attempts were made to model $\rho(T)$ of both compounds in terms of weak localization. Using the model of

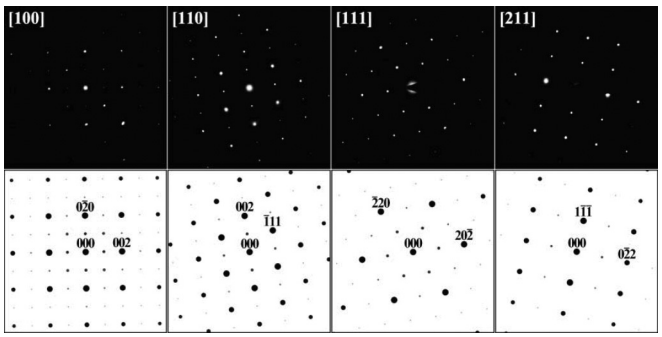

FIG. 2. TEM selected area diffraction patterns of low index zone axes [100], [110], [111], and [211] together with their simulations for unambiguously cubic $ThPt_3B$.

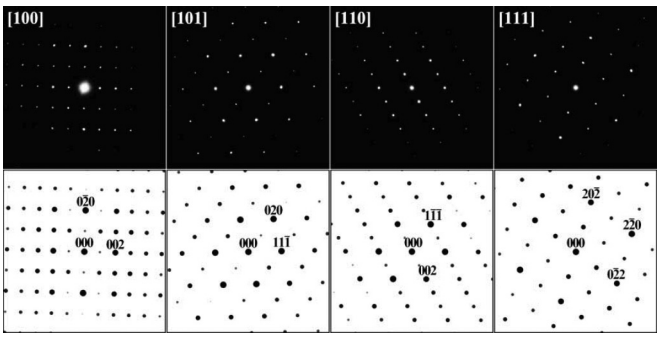

FIG. 3. TEM selected area diffraction patterns of low index zone axes [100], [101], [110], and [001] together with their simulations for tetragonal UPt_3B.

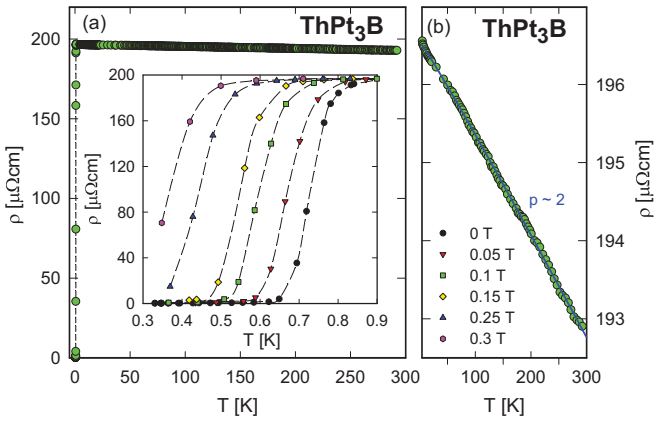

FIG. 4. (Color online) (a) Temperature dependent electrical resistivity ρ of $ThPt_3B$. The inset shows the field response of the superconducting transition measured at various externally applied magnetic fields [for clarity, the legend is collected in panel (b)]. (b) Normal state $\rho(T)$ data of $ThPt_3B$ at zero field. The solid line is a least squares fit as explained in the text.

Lee and Ramakrishnan, Ref. [23],

$$\sigma^{3D}(T) = \sigma_0 + \frac{e^2}{\hbar\pi^3}\frac{1}{a}T^{p/2}, \qquad (1)$$

we have fitted the data of Fig. 4(b), revealing $p \approx 2$. Here, σ^{3D} is the electrical conductivity of a three dimensional system ($\sigma \equiv 1/\rho$), σ_0 is inversely proportional to the residual resistivity, and the parameter a is some microscopic length scale in the problem, such as the inverse Fermi wave number. The exponent p is used to parametrize the temperature dependence of the inelastic scattering length L_i through $L_i \propto T^{-p/2}$. The value of p is usually between 1 (electron-electron scattering) and 2 (electron-phonon scattering); $p \approx 2$ refers to predominant electron-phonon scattering in $ThPt_3B$, rather than electron-electron scattering. Note, however, that the temperature variation up to room temperature is only about 2%.

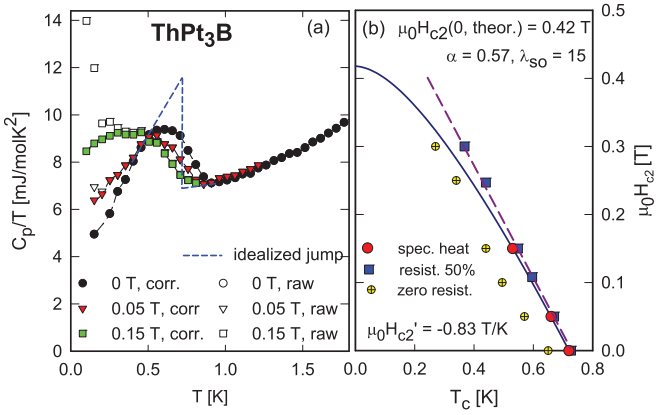

FIG. 5. (Color online) (a) Low temperature specific heat C_p of $ThPt_3B$ plotted as C_p/T vs T for various external magnetic fields. The dashed line sketches the idealized specific heat jump at $T = T_c$. (b) Temperature dependent upper critical field of $ThPt_3B$ as deduced from specific heat and resistivity measurements. The initial slope of the upper critical field, $\mu_0 H'_{c2}(T)$, is about -0.83 T/K (dashed line). The solid line corresponds to the WHH model, as explained in the text.

Figure 5(a) shows the low temperature heat capacity of $ThPt_3B$ as a function of external magnetic fields. In good agreement with resistivity data, the idealized specific heat jump [dashed lines, Fig. 5(a)] right at $T = T_c$ and in zero field arises at ≈ 0.75 K. This idealized jump of the specific heat, $\Delta C_p/T|_{T_c} \approx 5$ mJ/mol K^2, allows the calculation of $\Delta C_p/(\gamma_n T_c) \approx 1$, which is below the value expected from the Bardeen-Cooper-Schrieffer (BCS) theory [$\Delta C_p/(\gamma T_c) \approx 1.43$] [24]. An extrapolation of the zero field C_p/T data of the superconducting state towards $T \to 0$, however, reveals a residual Sommerfeld coefficient of about 3 to 4 mJ/mol K^2. This indicates that only a fraction of Fermi surface areas contributes to the formation of a superconducting state; additionally, a partial suppression of superconductivity could be provoked by local inhomogeneities and/or strain created by boron defects.

Switching on external magnetic fields shifts T_c to lower values, again in agreement with resistivity data. An upturn of C_p/T found experimentally at lowest temperatures and finite magnetic fields [open symbols, Fig. 5(a)] is attributed to the nuclear contribution of ^{195}Pt and is subtracted in terms of a standard T^{-2} contribution [closed symbols, Fig. 5(a)].

Figure 5(b) summarizes the temperature dependent upper critical field values $\mu_0 H_{c2}$ for $ThPt_3B$ as obtained from both resistivity and specific heat data. The initial slope $\mu_0 H'_{c2} = -0.83$ T/K exhibits an unexpectedly large range of linearity.

Essentially two mechanisms limit the value of $\mu_0 H_{c2}$: orbital pair breaking and Pauli limiting. Werthamer *et al.* [21] derived an expression (WHH model) for the upper critical field $\mu_0 H_{c2}$ in terms of orbital pair breaking, including the effect of Pauli spin paramagnetism and spin-orbit scattering. A comparison of experimental results with the WHH model is based on two parameters: α, the Pauli paramagnetic limitation (*Maki parameter*) and λ_{so} describing spin-orbit scattering. If the atomic numbers of the elements constituting the material increase, λ_{so} is expected to increase as well.

The Maki parameter α can be estimated from the Sommerfeld value γ and ρ_0 [21], $\alpha = (3e^2\hbar\gamma\rho_0)/(2m\pi^2 k_B^2)$, with e the electron charge and m the electron mass. Taking the experimental ρ_0 and γ yields $\alpha = 0.57$ for $ThPt_3B$. A value of similar magnitude can be derived from $\alpha = 5.3 \times 10^{-5}(\frac{-dH_{c2}(T)}{dT})|_{T=T_c}$ [25].

An increasing value of α reduces H_{c2} from its upper limit $h^* = H_{c2}/(T_c \partial\mu_0 H_{c2}/\partial T|_{T=T_c}) = 0.693$. Spin-orbit scattering, on the contrary, compensates for the decrease due to the paramagnetic limitation and restores $h^* \approx 0.693$ for $\lambda_{so} \to \infty$. Wong *et al.* [26] pointed out that λ_{so} is usually larger than 10 for 5*d* compounds, which also should hold for the present Th,Pt-based system. We have adjusted the WHH model to the experimental data [solid line in Fig. 5(b)], revealing $\lambda_{so} \approx 15$. Note, however, $H_{c2}(T \to 0)$, is quite insensitive for $\lambda_{so} > 10$. Although the best fit describes the high temperature $\mu_0 H_{c2}$ data reasonably well, the extremely extended linear dependency of $\mu_0 H_{c2}$ cannot be accounted for. It is interesting to mention that linearity of $\mu_0 H_{c2}(T)$ is a characteristic feature of amorphous materials as was demonstrated, e.g., by Johnson *et al.* [27]. The $\rho(T)$ behavior of $ThPt_3B$ (see Fig. 4) is supposed to be

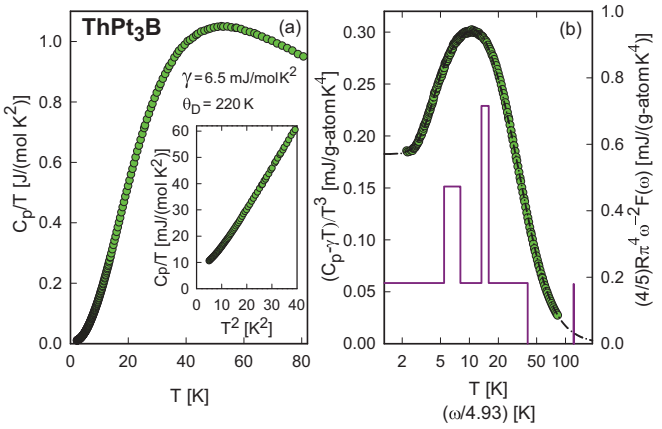

FIG. 6. (Color online) Temperature dependent specific heat C_p of $ThPt_3B$, (a) plotted as C_p/T vs T. The inset in (a) shows low temperature details; (b) plotted as $(C_p - \gamma T)/T^3$ vs $\ln T$. The dashed line is a least squares fit of the experimental data using the model described in the text. The essential parameters of the model used to construct the spectral function $F(\omega)$ (solid lines, right axis) are $\theta_D^\star = 199$ K, $\omega_{E1} = 33.3$ K with a width of ± 6.4 K, $\omega_{E2} = 72.1$ K with a width ± 6.2 K, and finally $\omega_{E3} = 600$ K with a width ± 10 K.

influenced from weak localization; thus it is in line with the general resistivity behavior of metals in the amorphic state.

The evidence of amorphic properties may be due to the peculiar elastic and vibrational state in which cubic $ThPt_3B$ is. This is indicated by the DFT derived harmonic phonon dispersions [see Fig. 7(a)] showing a massive amount of phonon branches with imaginary frequencies even starting from Γ.

Heat capacity data of $ThPt_3B$, taken in the normal state region, are plotted in Fig. 6(a) as C_p/T vs T. Approximating data at lowest temperatures by $C_p/T = \gamma T + \beta T^3$ yields the Sommerfeld coefficient $\gamma = 6.5$ mJ/mol K^2 and the Debye temperature $\theta_D^{LT} \simeq 220$ K [see inset, Fig. 6(a)].

As phonon dynamics is a key feature for the occurrence of BCS superconductivity, a detailed analysis of the specific heat following the model of Junod *et al.* [28,29] allows a definition of those phonon modes likely to be responsible for Cooper pairing. The quantitative modeling of the vibrational spectrum follows a procedure we have outlined in a number of previous papers (compare, e.g., Refs. [30,31]). Based on these considerations we have constructed an elementary phonon spectrum comprising a Debye density of states which accounts for the low temperature Debye temperature $\theta_D^{LT} \simeq 220$ K (see above) in combination with three additional, energetically separated Einstein-like modes, ω_{E1}, ω_{E2}, and ω_{E3}. The latter is included to account for the spectral weight of three optical branches related to the high frequency boron modes and preassigned as $\omega_{E3} = 600$ K. Different from the standard Einstein model of the specific heat, a certain frequency width $\Delta\omega$ and spectral weight for the branches ω_{E1} and ω_{E2} is allowed. Accordingly, a further parameter $\theta_D^\star$ is used to account for the remaining (fitable) spectral weight of the Debye component which is determined via the overall normalization of the spectral function, $g(\omega)$. The corresponding phonon heat capacity is calculated using

$$C_p(T) = R \int g(\omega) \frac{\left(\frac{1}{2}\frac{h\nu}{k_B T}\right)^2}{\sinh^2\left(\frac{1}{2}\frac{h\nu}{k_B T}\right)} d\omega, \qquad (2)$$

where ν is the phonon frequency, k_B the Boltzmann constant, h the Planck constant, and R the gas constant. Beside the high frequency mode, two low lying branches at around 33 ± 6.4 K and 72 ± 6.3 K are deduced from this model, responsible for deviations of experimental heat capacity data from the simple Debye model. The lowest Einstein-like branch could provide those phonons which couple with the electrons to form Cooper pairs.

In order to prove the predictions made above and explain the heat capacity from an atomistic point of view, the phonon dispersion and density of states was calculated applying DFT in terms of the software packages VASP and fPHON Refs. [6,7,13]. Results are shown in Figs. 7(a)–7(c).

The frequency dispersion of the vibrational modes in Fig. 7(a) reveals the instability of the cubic phase. A very large amount of frequencies are imaginary. In particular the imaginary branches at Γ are pointing at an elastic instability, which directly reflects the instability against the tetragonal distortion, as discussed previously. Particularly flat bands appear around 3 THz. High lying bands above 12 THz are attributed to vibrational modes of B. However, when allowing for anharmonic coupling at 100 K according to Refs. [14,15] the dispersions became all real (with the exception of a small region around Γ). Performing the anharmonic phonon calculations at temperatures below 100 K results in significantly varying frequency dispersions below 2 THz because of the occurrence of modes with imaginary frequencies. This finding elucidates the high sensitivity of the vibrational properties on temperature.

Figure 7(b) summarizes the phonon dispersion along high symmetry directions for tetragonal $ThPt_3B$. As already mentioned, DFT predicts a thermodynamically stable tetragonal structure which, according to Fig. 7(b), is also dynamically stable. The three high-frequency modes at about 12 and 16 THz are well separated from the acoustic and low lying optical branches. The latter form very flat bands, located between 2 and 4 THz. Linear acoustic branches arising at Γ indicate elastic stability.

Figure 7(c) shows the phonon density of states (PDOS) for both the harmonic and the anharmonic modeling of vibrations in the cubic structure as well as the results of the harmonic calculation for the tetragonal structure. For the cubic harmonic case there is no ω^2 Debye-like behavior at small frequencies because there are no linear acoustic branches detectable. Clearly, this property is connected to the massive amount of states with imaginary frequencies. According to the simplified Debye-Einstein model of Junod as applied to the measured specific heat in Fig. 6 two low lying Einstein modes at about 0.7 THz (33.3 K) and 1.5 THz (72.1 K) are extracted. The comparison with the calculated PDOS shows that in the DFT calculation only weak peaks occur in this frequency region. On the other hand, the very large Einstein-like peak at 2.5 THz and the smaller but still pronounced peak at 3.5 THz are not found by Junod's model. Presumably this discrepancy is attributable to the assumption of a Debye-like PDOS in the Junod model

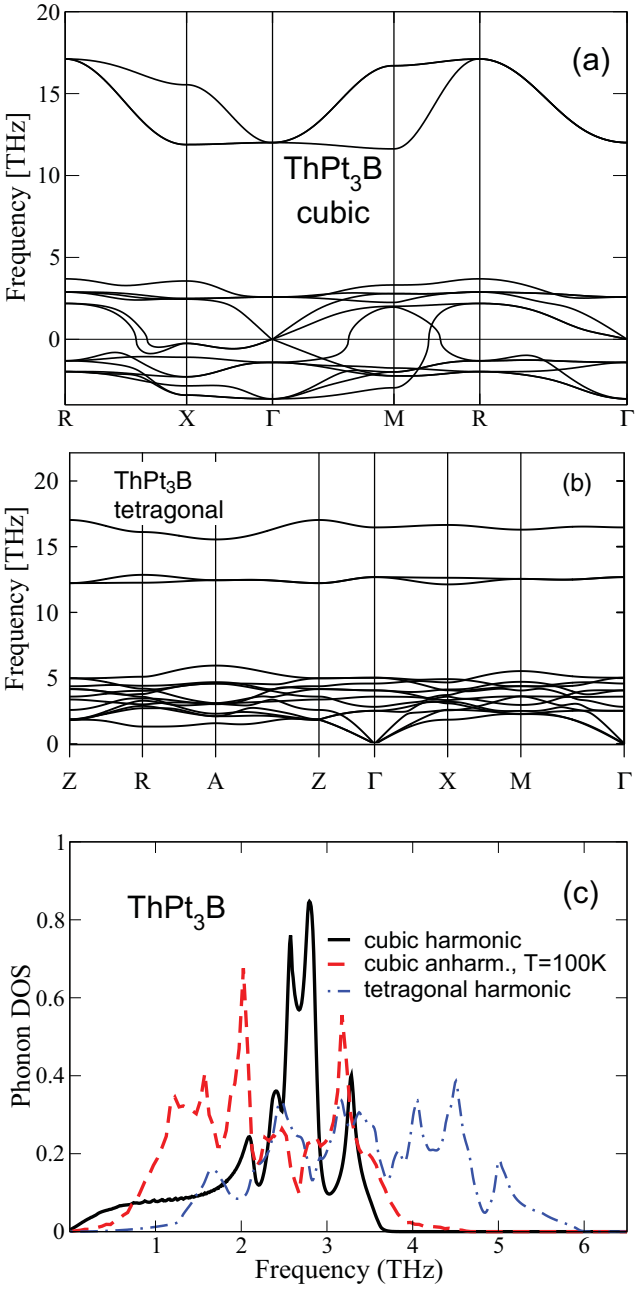

FIG. 7. (Color online) DFT calculated vibrational properties of $ThPt_3B$. (a) Phonon dispersion within the harmonic model along high symmetry directions for a cubic lattice. Imaginary frequencies are represented by negative values. (b) Phonon dispersion within the harmonic model along high symmetry directions for a tetragonal lattice. (c) Phonon density of states for the cubic harmonic (full black line), the anharmonic at 100 K model (red dashed line), and for the tetragonal structure (blue dashed-dotted line). The phonon densities of states are normalized to 1.

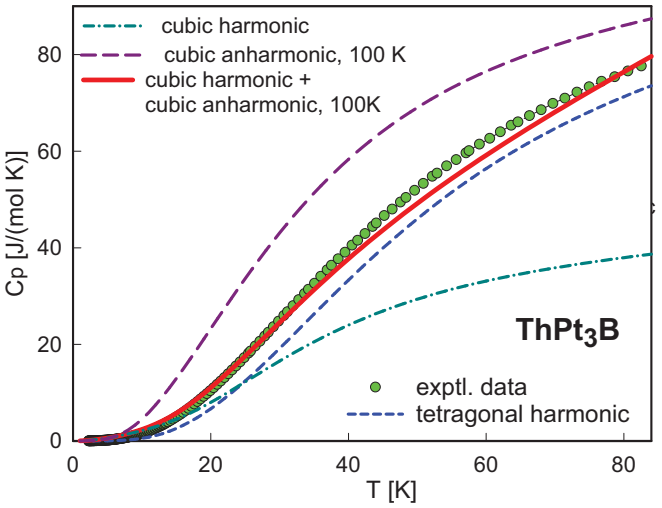

FIG. 8. (Color online) Temperature dependent specific heat C_p of $ThPt_3B$. Filled circles: experimental data points. DFT results for C_V of vibrations are shown by lines. Dark blue dashed: harmonic model for tetragonal structure; blue dash-dotted line: harmonic model for cubic compound (A); purple dashed line: anharmonic model at 100 K for cubic compound (B); red full line: linear interpolation according to $C_V(T) = [(100 - T)C_V(A) + TC_V(B)]/100$. The measured heat capacity C_p is derived at constant pressure, whereas from DFT the heat capacity at constant volume C_V is derived. The difference between these two quantities is neglected.

which is not the case for the DFT derived PDOS. There, the PDOS at low frequencies behaves rather like $\sqrt{\omega}$ than ω^2. A Debye-like PDOS is obtained for the anharmonic cubic case at 100 K and at 1.5 THz a broad peak arises reminiscent of the second Einstein mode in Junod's model at about 1.2 THz.

The PDOS of tetragonal $ThPt_3B$ exhibits a first prominent structure around 1.6 THz. Below about 1 THz, the PDOS closely follows a Debye-like behavior.

Taking into account Eq. (2), the heat capacity can be calculated from the PDOS obtained from the DFT calculations [Fig. 7(c)]. It should be noted that the PDOS shown in Fig. 7(c) are all normalized to 1. Therefore, when states with imaginary frequencies appear (as it is the case for cubic $ThPt_3B$), the PDOS has to be renormalized if it is used for calculating thermodynamical vibrational properties such as C_V. In this work, C_V for cubic $ThPt_3B$ in Fig. 8 is derived from the spectrum of real frequencies. Results are plotted in Fig. 8 together with the experimental data. Considering cubic $ThPt_3B$ the two DFT derived curves shown describe the experimental data very badly. For the harmonic approximation $C_V(T)$ is far too small with increasing temperature because of the vibrational states with imaginary frequencies which are not included. For the anharmonic approximation $C_V(T)$ is significantly too large. This calculation is done at 100 K and therefore only $C_V(T = 100\ \mathrm{K})$ should be compared to experiment. However, by a simple linear interpolation with respect to T—as defined in the caption of Fig. 8—a well-fitting result (red curve in Fig. 8) is obtained. This corroborates the claimed thermodynamically and dynamically unstable cubic structure of $ThPt_3B$.

The heat capacity in the displayed temperature range for thermodynamically stable tetragonal $ThPt_3B$ is smaller than the experimental result. Presumably, this is due to the more pronounced Debye-like behavior of the low-frequency PDOS.

From electronic structure calculations a number of normal state properties of $ThPt_3B$ are derived. Figure 9 shows

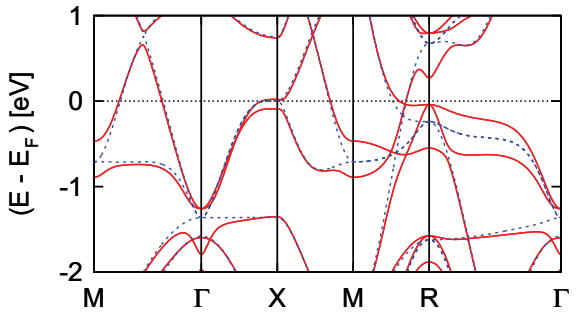

FIG. 9. (Color online) Electronic band structure of cubic $ThPt_3B$ referring to the scalar-relativistic calculation omitting spin-orbit coupling (blue dashed lines) and to the fully relativistic calculation including spin-orbit coupling (red solid lines).

the electronic structure of cubic $ThPt_3B$ calculated scalar-relativistically (no spin-orbit coupling, blue dashed line) as well as fully relativistically (with spin-orbit coupling, red solid lines). The electronic structure depicted around the Fermi energy E_F along high symmetry directions reveals several bands which intersect the Fermi energy as a signature of a metallic state of this compound.

The calculation with spin-orbit interaction reveals a splitting of bands at all high-symmetry points, in particular at the $\vec{k}$ points X and R for which this splitting induced by the spin-orbit coupling is observed close to the Fermi energy. Specifically around R, flat bands are moved very close to the Fermi energy by the spin-orbit coupling, resulting in a narrow peak in the density of states just below E_F (see also Fig. 11). A small reduction of the valence electron number by B vacancies would shift E_F into this peak. However, a double (spin) degeneracy of the energy bands remains throughout the Brillouin zone as the cubic crystal structure does have a center of inversion.

The Fermi surface in Fig. 10 shows a very interesting extending flat cross section perpendicular to the direction $\Gamma - M$ at about $0.4 \times \overline{\Gamma\text{-}M}$. Obviously, these cross sections offer extensive Fermi surface nesting for phonon states with wave vectors $\vec{q} \approx 0.8 \times \overline{\Gamma\text{-}M}$. It should be noted that all such vectors related by cubic symmetry are of equal importance for the nesting. Indeed, soft phonon modes in direction $\Gamma - M$ are found close to M, in particular the lowest branch reaching M at about 2 THz, rising from the pool of imaginary frequencies. Such phonon modes would be suitable to couple the Fermi surface sheets as shown in Fig. 10 and thus maintain superconductivity.

The electronic density of states (DOS) have been calculated (Fig. 11) for the fully relativistic case for the cubic (upper panel) and tetragonal (lower panel) crystal structure. Local DOS of the constituent elements are shown in various colors. The DOS value at E_F of 2.7 states/eV is the same for both structures, mainly built up by the Pt-like local DOS. For the cubic structure the local DOS of Th and B are almost negligible. Around 1 eV below the Fermi energy a pseudogap is present for cubic $ThPt_3B$, which is less pronounced for the tetragonal structure.

The DOS at Fermi energy derived from the present DFT calculations of 2.7 states/eV corresponds to a bare Sommerfeld

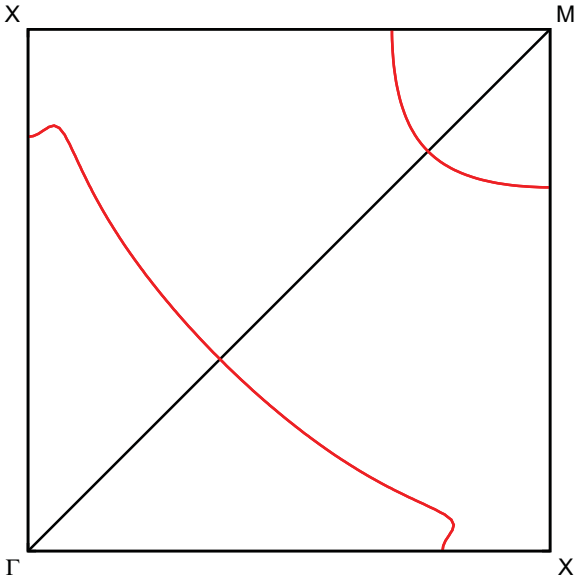

FIG. 10. (Color online) Fermi surface of cubic $ThPt_3B$ referring to the fully relativistic calculation. The corner points (in units of $2\pi/a$) are $\Gamma(0\,0\,0)$, $X(1/2\,0\,0)$, $M(1/2\,1/2\,0)$, and $X(0\,1/2\,0)$.

value of $\gamma_b = 6.4$ mJ/mol K^2, which does not take any correlations or enhancement factors into account. The same value would be obtained if E_F moves down by about 0.2 eV due to the occurrence of B vacancies corresponding to a reduction of the number of valence electrons by 0.15 states (or 5% less B). The experimental $\gamma = 6.5$ mJ/mol K^2 is almost matching the bare value, thus indicating a rather weak electron-phonon enhancement factor when referring to the idealized structure.

Within the McMillan model [32], the superconducting transition temperature T_c is given by

$$T_c = \frac{\theta_D}{1.45} \exp\left[\frac{-1.04(1+\lambda)}{\lambda - \mu_c^*(1+0.62\lambda)}\right], \qquad (3)$$

where λ is the dimensionless electron-phonon coupling constant, related in terms of the Eliashberg theory to the phonon density of states. λ determines the attractive part of the Cooper pair bonding, while μ^* is the repulsive screened Coulomb part, usually set to ≈ 0.13. Applying this simple model yields $\lambda = 0.46$, classifying $ThPt_3B$ as a superconductor in the weak coupling limit.

In the following section a number of parameters derived from an analysis of superconducting and normal state properties are presented.

An integration of the entropy difference from the superconducting (s) and the normal (n) state yields the difference of the free energies, $F_n - F_s = \delta F$, being proportional to the thermodynamic critical field, i.e.,

$$\delta F(T) = \frac{\mu_0 H_c^2(T)}{2} = \int_{T_c}^{T} \int_{T_c}^{T'} \frac{C_s - C_n}{(T'')} dT'' dT' \qquad (4)$$

revealing $\mu_0 H_c \approx 6$ mT when extrapolating towards $T = 0$.

From the thermodynamic critical field, the dimensionless Ginzburg-Landau parameter $\kappa_{GL} = H_{c2}(0)/(\sqrt{2}H_c) \approx 43$ is calculated. The upper critical field $\mu_0 H_{c2}(0) = 0.42$ T

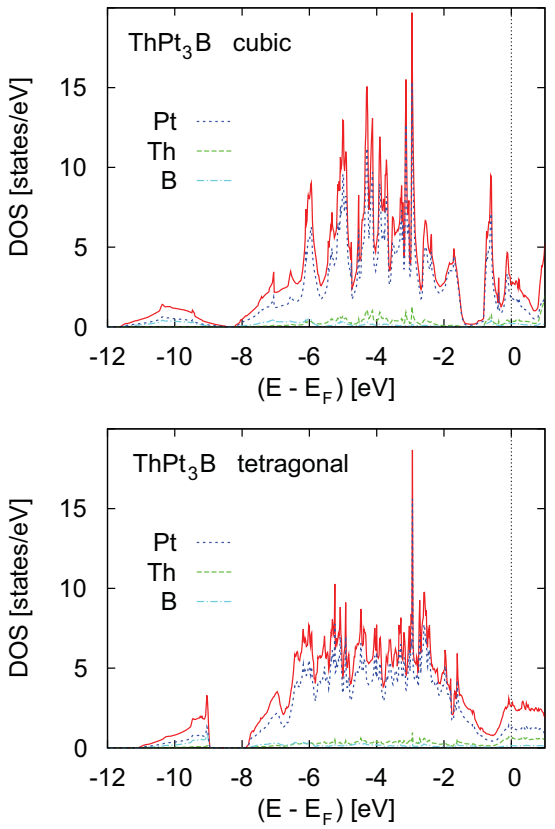

FIG. 11. (Color online) Total and site-projected electronic density of states (DOS) of $ThPt_3B$ for the cubic (upper panel) and the tetragonal structure (lower panel) for the fully relativistic calculation.

has been taken from the WHH fit [compare Fig. 5(a)]. The coherence length $\xi_0 \simeq 2.8 \times 10^{-8}$ m is obtained from $\mu_0 H_{c2} = \Phi_0/(2\pi\xi_0^2)$, with Φ_0 being the flux quantum. Combining the Ginzburg-Landau parameter with the coherence length, the London penetration depth results in $\lambda_L(T \to 0) \simeq 1.3 \times 10^{-6}$ m.

In the standard BCS scenario [33], where quantities like the Sommerfeld value, the residual resistivity, and the slope of the upper critical magnetic field enter the calculations ($\gamma = 6.5$ mJ/mol K^2, $\mu_0 H'_{c2} = -0.83$ T/K, and $\rho_0 = 196$ $\mu\Omega$ cm), similar parameters for ξ, κ, and λ were obtained. The ability of model calculations in this framework can be seen, e.g., from the slope of the upper critical field which reads $|\mu_0 H'_{c2}| = 4490\gamma\rho_0 = 0.867$ T/K, in almost perfect agreement with the experimental result, 0.83 T/K. The mean free path of electrons within this model is obtained as $l_{tr} \approx 1.56 \times 10^{-8}$ m. From $l_{tr}/\xi \approx 0.55$ we classify $ThPt_3B$ as a superconductor in the dirty limit; the value of κ of the order of 40 refers to an extreme type II superconductor.

F. Nonsuperconducting UPt_3B

We have studied $\rho(T)$ of UPt_3B down to 340 mK. From resistivity measurements neither a superconducting nor a magnetic phase transition was observed. In contrast to $ThPt_3B$ metallic resistivity behavior was found in the entire temperature range. However, $\rho(T)$ does not follow a simple metallic behavior; rather, at lowest temperatures a behavior according

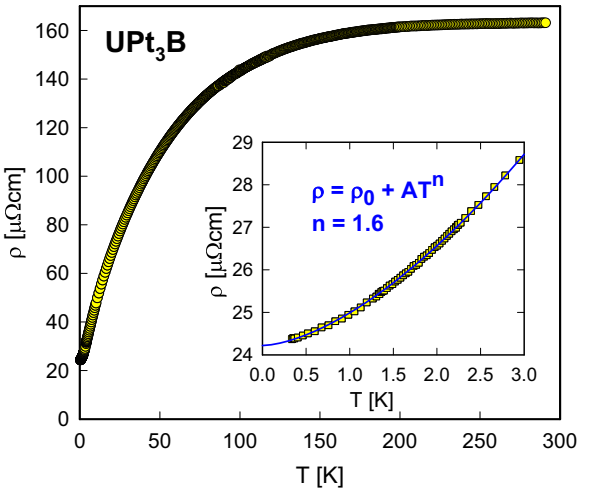

FIG. 12. (Color online) Temperature dependent resistivity ρ of UPt_3B. The inset shows low temperature details and the solid line is a least squares fit based on $\rho = \rho_0 + AT^n$ with $n = 1.6$.

to $\rho = \rho_0 + AT^n$ with $n = 1.6$ is observed (see Fig. 12). The latter refers to distinct deviations from a Fermi liquid ground state due to pronounced spin fluctuations, which are evident also from the large value of the Sommerfeld coefficient $\gamma = 221$ mJ/mol K^2. Moreover, archetypal spin fluctuation systems like YCo_2 exhibit at elevated temperatures a tendency towards saturation, which is also evident from Fig. 12.

The temperature dependent specific heat C_p of UPt_3B is plotted in Fig. 13 as C_p/T vs T. The absence of any low temperature anomalies evidences the lack of a phase transition, in agreement with the $\rho(T)$ data discussed above. The inset in Fig. 13 shows C_p for T below 15 K. A standard procedure to isolate the magnetic contribution via subtraction of $C_p(T)$ of nonmagnetic $ThPt_3B$ is not meaningful for nonisotypic structure types. A fit of the low temperature data of UPt_3B with the simple ansatz, $C_p(T) = \gamma T + \beta T^3 + \delta T^3 \ln(T/T^*)$,

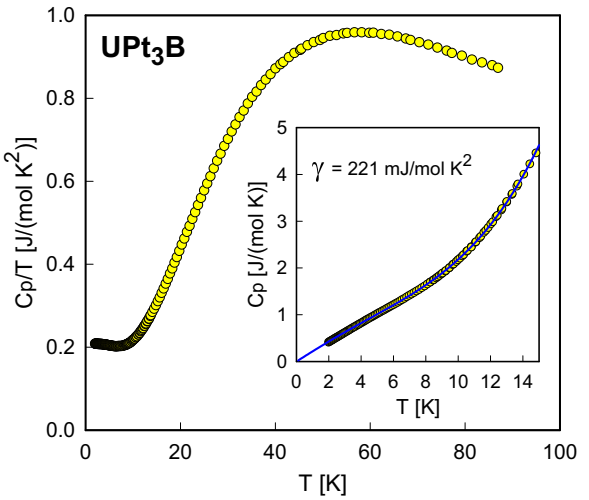

FIG. 13. (Color online) Temperature dependent specific heat C_p of UPt_3B plotted as C_p/T vs T. The inset shows low temperature details and the solid line is a least squares fit based on a spin fluctuation model.

where the latter term accounts for spin fluctuations reveals excellent agreement for $\gamma = 221$ mJ/mol K^2 and $T^* = 22$ K (solid line, inset Fig. 13), suggesting spin fluctuations in the nearly localized regime. As our DFT derived DOS at the Fermi energy is 6.3 states/eV, corresponding to 14.94 mJ/mol K^2, the substantially larger value observed from the experiment is significantly enhanced by spin fluctuations. Assuming a moderate value of an electron-phonon enhancement $1 + \lambda_{e,ph} \approx 1.3$ to 1.5, the remaining electron-spin fluctuation enhancement factor $\lambda_{e,\mathrm{spin}}$ would be of the order of 10 to 15, a typical value for spin fluctuation systems like UAl_2, with $\lambda_{e,\mathrm{spin}} = 15.6$ [34].

Taking into account spin polarization, DFT results in a total magnetic moment of 1.0 μ_B for ferromagnetic ordering, which breaks down for small changes in volume. This finding corroborates the argument that UPt_3B is close to a magnetic instability.

V. SUMMARY

The compounds $AnPt_3B$ have been characterized from x-ray and TEM data: perovskite-type $ThPt_3B$ [$a = 0.4383(2)$ nm; $Pm\bar{3}m$] and UPt_3B [$a = 0.38906(3)$ and $c = 0.52241(5)$ nm; $P4mm$] isotypic with the noncentrosymmetric structure of $CePt_3B$. A study of bulk properties carried out on $ThPt_3B$ revealed a superconducting ground state below 0.75 K. Although DFT calculations achieve stable solutions for the tetragonal noncentrosymmetric $CePt_3B$ structure rather than for the cubic $CaTiO_3$-type of structure, x-ray, TEM, and heat capacity studies unambiguously confirm the latter type. Normal state properties of metallic $ThPt_3B$ are characterized by an unusual temperature dependent electrical resistivity, decreasing almost linearly above T_c with increasing temperature. Weak localization due to disorder in the material (e.g., vacancies at the B sites) would straightforwardly explain such a feature. Moreover, comparing the Th and the U-based residual resistivity ratios also reveal a huge difference, about 1 to 8, respectively. This observation suggests a significantly larger amount of structural defects (e.g., boron vacancies) in $ThPt_3B$, presumably stabilizing the cubic structure via a strain compensation mechanism.

Bulk superconductivity in $ThPt_3B$ is supported by heat capacity results. Although the Maki parameter, $\alpha = 0.57$, is well above zero, Pauli limiting does not occur, referring to spin-singlet pairs in the superconducting condensate. $ThPt_3B$ is a type II superconductor in the dirty limit.

For cubic $ThPt_3B$ DFT calculations for the vibrational properties reveal a large amount of nonvibrating modes with imaginary frequencies. This finding is the consequence of the structural instability of the cubic compound. Relativistic DFT calculations predict appropriate Fermi surface features by which Cooper pairs could be created, because suitable phonon states are found in the calculated phonon dispersion. The measured specific heat data up to 80 K are reasonably well described by the DFT calculation for the vibrational properties interpolating the DFT results at 0 K with calculations for anharmonic coupling at 100 K.

Tetragonal noncentrosymmetric UPt_3B does not exhibit superconductivity or long range magnetic order above 340 mK. Rather, a spin fluctuation scenario with a remarkably large Sommerfeld value, $\gamma = 221$ mJ/molK^2, characterizes the metallic state of this compound. DFT calculations confirm the tetragonal structure and the occurrence of small weakly coupled magnetic moments. The good agreement between experiment and DFT concerning the ground state tetragonal structure of UPt_3B gives confidence in the applied procedures. Since the same techniques were applied to $ThPt_3B$ it is plausible that distinct mechanisms, not accounted for in terms of DFT, stabilize the cubic structure of $ThBPt_3$.

ACKNOWLEDGMENTS

Research supported by the Austrian Science Foundation FWF, Projects No. 22295 and No. 24380. P.R. is grateful for support by Sacavem within the action COST-P16. The DFT calculations were done on the Vienna Scientific Cluster (VSC).

[1] E. Bauer, G. Hilscher, H. Michor, C. Paul, E.-W. Scheidt, A. Gribanov, Y. Seropegin, H. Noël, M. Sigrist, and P. Rogl, Phys. Rev. Lett. **92**, 027003 (2004).
[2] E. Bauer and M. Sigrist, *Non-Centrosymmetric Superconductors: Introduction and Overview*, Lecture Notes in Physics Vol. 847 (Springer-Verlag, Berlin, 2012).
[3] J. Rodriguez-Carvajal, Physica B (Amsterdam) **192**, 55 (1993).
[4] E. Bauer, S. Berger, C. Paul, M. D. Mea, G. Hilscher, H. Michor, M. Reissner, W. Steiner, A. Grytsiv, P. Rogl, and E. W. Scheidt, Phys. Rev. B **66**, 214421 (2002).
[5] R. Bachmann, F. J. DiSalvo Jr., T. H. Geballe, R. L. Greene, R. E. Howard, C. N. King, H. C. Kirsch, K. N. Lee, H.-U. T. R. E. Schwall, and R. B. Zubeck, Rev. Sci. Instrum. **43**, 205 (1972).
[6] G. Kresse and J. Furthmüller, Phys. Rev. B **54**, 11169 (1996).
[7] G. Kresse and D. Joubert, Phys. Rev. B **59**, 1758 (1999).
[8] P. E. Blöchl, Phys. Rev. B **50**, 17953 (1994).
[9] D. M. Ceperley and B. J. Alder, Phys. Rev. Lett. **45**, 566 (1980).
[10] J. P. Perdew and A. Zunger, Phys. Rev. B **23**, 5048 (1981).
[11] H. Monkhorst and J. Pack, Phys. Rev. B **13**, 5188 (1976).
[12] K. Hummer, A. Grüneis, and G. Kresse, Phys. Rev. B **75**, 195211 (2007).
[13] D. Alfè, Comput. Phys. Commun. **180**, 2622 (2009).
[14] P. Souvatzis, O. Eriksson, M. I. Katsnelson, and S. P. Rudin, Phys. Rev. Lett. **100**, 095901 (2008).
[15] P. Souvatzis, O. Eriksson, M. Katsnelson, and S. Rudin, Comput. Mater. Sci. **44**, 888 (2009).
[16] O. Sologub, P. Rogl, E. Bauer, G. Hilscher, H. Michor, E. Royanian, G. Giester, and A. P. Goncalves, J. Phys.: Condens. Matter **22**, 125601 (2010).
[17] D. Lerch, O. Wieckhorst, G. Hart, R. Forcade, and S. Mueller, Modell. Simul. Mater. Sci. Eng. **17**, 055003 (2009).
[18] I. Loe, I. McColm, and T. Quigley, J. Less-Common Met. **46**, 217 (1976).

[19] J. P. Perdew, K. Burke, and M. Ernzerhof, Phys. Rev. Lett. **77**, 3865 (1996).
[20] P. Stadelmann, JEMS-EMS java version, 2014, URL http://cimewww.epfl.ch/people/stadelmann/jemsWebSite/jems.html.
[21] N. R. Werthamer, E. Hefland, and P. C. Hohenberg, Phys. Rev. **147**, 295 (1966).
[22] T. Khan, E. Royanian, H. Michor, A. Gribanov, P. Rogl, and E. Bauer (in preparation).
[23] P. A. Lee and T. V. Ramakrishnan, Rev. Mod. Phys. **57**, 287 (1985).
[24] J. Bardeen, L. N. Cooper, and J. R. Schrieffer, Phys. Rev. **108**, 1175 (1957).
[25] K. Maki, Phys. Rev. **148**, 362 (1966).
[26] K. M. Wong, E. J. Cotts, and S. J. Poon, Phys. Rev. B **30**, 1253 (1984).
[27] W. L. Johnson, S. J. Poon, and P. Duwez, Phys. Rev. B **11**, 150 (1975).
[28] A. Junod, D. Bichsel, and J. Müller, Helv. Phys. Acta **52**, 580 (1979).
[29] A. Junod, T. Jarlborg, and J. Müller, Phys. Rev. B **27**, 1568 (1983).
[30] E. Bauer, A. Grytsiv, X.-Q. Chen, N. Melnychenko-Koblyuk, G. Hilscher, H. Kaldarar, H. Michor, E. Royanian, G. Giester, M. Rotter, R. Podloucky, and P. Rogl, Phys. Rev. Lett. **99**, 217001 (2007).
[31] A. Grytsiv, X.-Q. Chen, N. Melnychenko-Koblyuk, P. Rogl, E. Bauer, G. Hilscher, H. Kaldarar, H. Michor, E. Royanian, R. Podloucky, M. Rotter, and G. Giester, J. Phys. Soc. Jpn. **77**, 121 (2008).
[32] W. L. McMillan, Phys. Rev. **167**, 331 (1968).
[33] T. P. Orlando, E. J. McNiff, S. Foner, and M. R. Beasley, Phys. Rev. B **19**, 4545 (1979).
[34] K. Ikeda, S. K. Dhar, M. Yoshizawa, and K. A Gschneidner Jr., J. Magn. Magn. Mater. **100**, 292 (1991).